Hindawi
International Journal of Rotating Machinery
Volume 2019, Article ID 4675286, 19 pages
https://doi.org/10.1155/2019/4675286

Research Article

Development and Experimental Validation of Auxiliary Rolling Bearing Models for Active Magnetic Bearings (AMBs) Applications

Anna Tangredi,[1] Enrico Meli,[1] Andrea Rindi,[1] Alessandro Ridolfi,[1] Pierluca D'Adamio,[1] Amedeo Frilli,[1] Duccio Fioravanti,[2] and Benjamin Defoy[3]

[1]*Department of Industrial Engineering (DIEF), University of Florence, Via di S. Marta 3, Florence, Italy*
[2]*Senior Engineer Ph.D. BHGE, Lead R&D Engineer BHGE, Italy*
[3]*Senior Engineer Ph.D. BHGE, Lead R&D Engineer BHGE, France*

Correspondence should be addressed to Enrico Meli; enrico.meli@unifi.it

Received 28 September 2018; Revised 11 January 2019; Accepted 18 February 2019; Published 1 April 2019

Academic Editor: Hyeong Joon Ahn

Nowadays, the search for increasing performances in turbomachinery applications has led to a growing utilization of active magnetic bearings (AMBs), which can bring a series of advantages thanks to their features: AMBs allow the machine components to reach higher peripheral speeds; in fact there are no wear and lubrication problems as the contact between bearing surfaces is absent. Furthermore, AMBs characteristic parameters can be controlled via software, optimizing machine dynamics performances. However, active magnetic bearings present some peculiarities, as they have lower load capacity than the most commonly used rolling and hydrodynamic bearings, and they need an energy source; for these reasons, in case of AMBs overload or breakdown, an auxiliary bearing system is required to support the rotor during such landing events. During the turbomachine design process, it is fundamental to appropriately choose the auxiliary bearing type and characteristics, because such components have to resist to the rotor impact; so, a supporting design tool based on accurate and efficient models of auxiliary bearings is very useful for the design integration of the Active Magnetic Bearing System into the machine. This paper presents an innovative model to accurately describe the mechanical behavior of a complete rotor-dynamic system composed of a rotor equipped with two auxiliary rolling bearings. The model, developed and experimentally validated in collaboration with *Baker Hughes a GE company* (providing the test case and the experimental data), is able to reproduce the key physical phenomena experimentally observed; in particular, the most critical phenomenon noted during repeated experimental combined landing tests is the rotor forward whirl, which occurs in case of high friction conditions and greatly influences the whole system behavior. In order to carefully study some special phenomena like rotor coast down on landing bearings (which requires long period of time to evolve and involves many bodies and degrees of freedom) or other particular events like impacts (which occur in a short period of time), a compromise between accuracy of the results and numerical efficiency has been pursued. Some of the elements of the proposed model have been previously introduced in literature; however the present work proposes some new features of interest. For example, the lateral and the axial models have been properly coupled in order to correctly reproduce the effects observed during the experimental tests and a very important system element, the landing bearing compliant suspension, has been properly modelled to more accurately describe its elastic and damping effects on the system. Furthermore, the model is also useful to characterize the frequencies related to the rotor forward whirl motion.

1. Introduction

Rotors equipped with AMBs technology have the advantage to allow the machine to reach high performances, but a secondary rolling bearings system is required, because magnetic bearings are not able to support the rotor in case of overload or failure of the energy supply system. Such auxiliary bearings system, whose main elements are catcher bearings, is directly engaged during rotor landings; thus, in order to safely support the rotor, it must have very high mechanical and dynamical properties in order to guarantee the desired impact, thermal, and wear resistance. The landing system shall also be able to protect the rotor from possible damage and guarantee long service life; for these reasons, the development of a tool able to

represent such rotor-dynamic systems and based on efficient rolling bearing models is useful to provide an appropriate support during the design phase.

The current work presents an improved auxiliary bearing system model with a FEM rotor model able to represent real system dynamic behavior and to reproduce the key effects observed during experimental tests. The model is able to predict the behavior of the complete system during transient, steady and emergency conditions (e.g., delevitation and landing phenomena) and it is composed of different submodels: the rotor submodel, which includes a FEM model to represent the lateral dynamic of the rotor and two rigid body models to reproduce axial and torsional rotor dynamics, and the auxiliary rolling bearing submodel, characterized by a combination of multibody and contact models able to represent the dynamics and the interactions of the auxiliary system elements.

The model has been developed and experimentally validated in collaboration with *Baker Hughes a GE company* which provided the system layout data and the results of the experimental tests performed on a dedicated scale test rig (Section 2.5).

In this paper, a comparison between the most significant experimental and simulated results is presented; through the analysis of the results, it is possible to observe a satisfying reproduction of the real system behavior. Real rotor displacements, auxiliary bearing elements displacements, interaction forces and moments, whirling frequencies, rotor, and bearing speeds and acceleration are very well represented by the simulated results thanks to the optimal calibration of the model parameters.

Rotating system behavior has been studied extensively in the past by many researchers. Szcygielski [1] conducted one of the initial studies concerning a high-speed rotor touching a rigid body, modelling the rotor like a gyro pendulum; the preliminary analytical results showed a good representation of the experimental trajectories of the gyro axis.

Among many researchers, Muszynska [2], Beatty [3], and Ehrich [4] studied the rubbing phenomena, revealing that the rotating systems show nonlinear dynamical behavior such as sub- and super-synchronous responses and even chaotic motion.

Other researchers investigated theoretically and experimentally the dry friction backward whirl motion; Bartha [5, 6] observed that, during rotor impact and rub phenomena, the rotor vibration shows backward orbiting due to the presence of a tangential friction force.

Wilkes et al. [7] investigated, through experimental and numerical methods, the nature of multimode dry friction whip and whirl for a variety of rub materials and clearances; their experimental results showed multiple whirl and whip regions.

In order to reduce rubbing and the related phenomena, Lahriri et al. [8] proposed new backup bearing design, using special pins to center the rotor during impacts and mitigate its lateral motion. Furthermore, they developed a mathematical model to capture phenomena arising from rotor impacts.

Schmied and Pradetto [9] studied the behavior of a rotor landing onto auxiliary bearings and developed a numerical predictive model: simulation results reproduced a fully backward whirl rotor orbit for a few rotations, until the auxiliary bearing reached the rotor speed.

Other researches focus on the steady-state responses of rotor-dynamic systems: H. Xie et al. [10] studied a complex rotor system supported by auxiliary bearings with clearance at each end of the rotor. The influence of rotor imbalance, clearance, support stiffness, and damping has been investigated using direct numerical integration of the governing equation of motion and the harmonic balance method.

L. Della Pietra et al. [11] studied and experimentally investigated the static and the dynamic behavior of a rigid balanced rotor on journal bearings; the conducted study underlined the importance of the static behavior of the rotor bearing system for a correct interpretation of some aspect of the dynamic behavior. In fact they observed that a small dynamic imbalance can significantly modify the rotor-dynamic behavior inducing a whirl with large orbits.

Other researchers designed innovative auxiliary bearings. Hawkins et al. [12] and McMullen et al. [13] have performed endurance tests, testing different variety of bearings and landing sleeves materials in order to improve the design of the auxiliary system. They observed excessive wearing of the thrust washer and concluded that a thrust surface with lower friction coefficient could provide better performance.

M. Dougdag et al. [14] carried out an experimental verification of a simplified model of a ball bearing in both static and dynamic modes and test its capabilities to simulate accurately fault effects; the developed model considers the balls scrolling in the cage and the effect of the load rotating vector.

Ransom et al. [15] and Masala et al. [16] performed experimental tests and developed specific numerical model on a scaled and a full scale AMB supported subsea compressor.

R. G. Kirk [17] analysed AMB turbomachinery applications concerning the operation of the rotor drop onto the auxiliary bearings. His studies focused on the selection of specific auxiliary bearings able to withstand the contact forces following the speed rotor drop. The proper design of AMB machinery requires the calculation of the anticipated loading for the auxiliary bearings; so, Kirk presented results of transient response evaluation of a full-size compressor rotor to illustrate some of the important parameters in the design for rotor drop.

In another research E.E. Swanson et al. [18] studied in detail the dynamic behavior of the rotor/bearing/support systems in the case of total loss of AMB support. They presented test results for the initial rotor drop transient for several backup bearing configurations. The cases reported are rigidly mounted antifriction bearing, rigidly mounted solid bushings (lubricated and unlubricated), and two soft mounted solid bushing configurations.

Other researchers like J. Wilkes et al. [19] observed strong circular forward whirl following an AMB failure and developed specific models to reproduce such phenomenon. They developed an innovative model of auxiliary bearing system that represents a great step forward in the reproduction of rotor-dynamic system behavior; in fact the model allows reproducing the forward whirl rotor orbit observed during

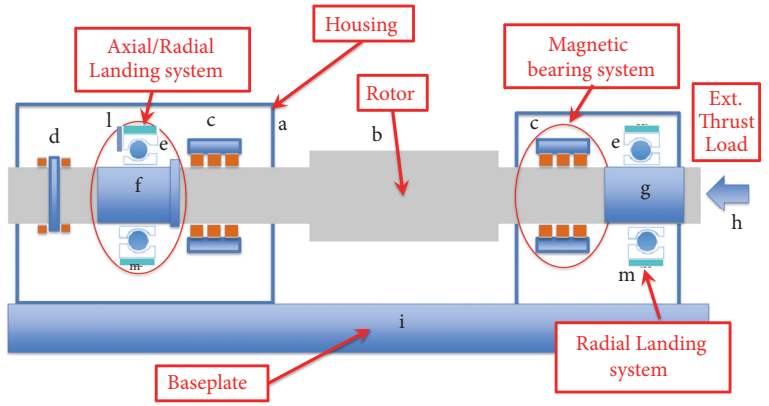

Figure 1: General scheme of a magnetic bearings supported rotor with its auxiliary landing system.

the landing tests. The model is based on a formulation where a friction force between the axial face of the rotor sleeve and the thrust face of the catcher bearing has been included.

The model proposed in this research work represents an efficient and flexible tool, able to reproduce the behavior of the whole system and the physical phenomena connected to the auxiliary rolling bearings system (e.g., forward whirl). A compromise between accuracy of the results and numerical efficiency is mandatory, in order to carefully study some interesting phenomena like the rotor full coast down on landing bearings, which requires long period of time to evolve and involves many bodies and degrees of freedom, and particular events like impulsive forces which occur in a very short period of time.

The present work proposes some innovative features of interest; the new formulation takes into account the reciprocal coupling between the lateral and the axial rotor-dynamic models, enabling the reproduction of the forward whirl observed in the radial dynamics and the oscillatory axial behavior of the system during the whirling phenomenon. The elastic and damping elements of the compliant axial and radial auxiliary bearing suspension have been modelled taking into account their features and their influence on the whole system behavior.

The developed model can simulate the rotor dynamics in presence of different unbalances and represent the behavior of the whole system under different operating conditions: rotor constant speed, rotor decelerated speed, and different axial load profiles; it also includes the estimation of power and energy losses, so it can be used as an effective supporting tool for the machine designer to foresee the main sources of power losses. Furthermore the model is also useful to characterize the frequencies related to some characteristic phenomena of the system, like the backward and forward oscillation frequencies of the machine components.

2. Materials and Methods

In this Section the architecture of the rotor-dynamic system (Figure 2) is described and the structure of the developed numerical model is presented; Section 2.3 is dedicated to the description of the auxiliary bearing system and the dynamic and contact models developed to represent the bearing elements behavior.

2.1. General Architecture. The rotor-dynamic system represented in the numerical model is composed of a rotor supported by two radial and one axial magnetic bearings and equipped with an auxiliary bearing system based on two rolling bearings (Figure 1).

The main elements of the system, which are represented into the Matlab-Simulink model, are

(1) housing (a);
(2) rotor (b);
(3) two radial active magnetic bearings (AMBs) (c);
(4) one axial active magnetic bearing (AMB) (d);
(5) two auxiliary rolling bearings (e);
(6) radial rotor landing sleeve (f);
(7) axial and radial rotor landing sleeve (g);
(8) force actuator for the application of the axial load (h);
(9) baseplate (i);
(10) the axial support for the landing system (l);
(11) an elastic-damping element for each bearing, the ribbon damper (m).

Between the rotor sleeve and the catcher bearings a radial clearance is present: in emergency conditions, the rotor passes through the radial clearance, lands on the inner rings of the catcher bearings, and continues to rotate supported by the auxiliary system.

The real rotor-dynamic system is equipped with a force actuator which applies an external axial thrust load on the nondrive end of the system; at this side of the system there is also an axial clearance between the rotor sleeve and the auxiliary bearing; under the axial thrust, the rotor translates along its symmetry axis.

Between the outer race and the housing specific elastic elements (Figure 1) are placed: the axial support for the bearing and the elastic ribbon damper. The axial support

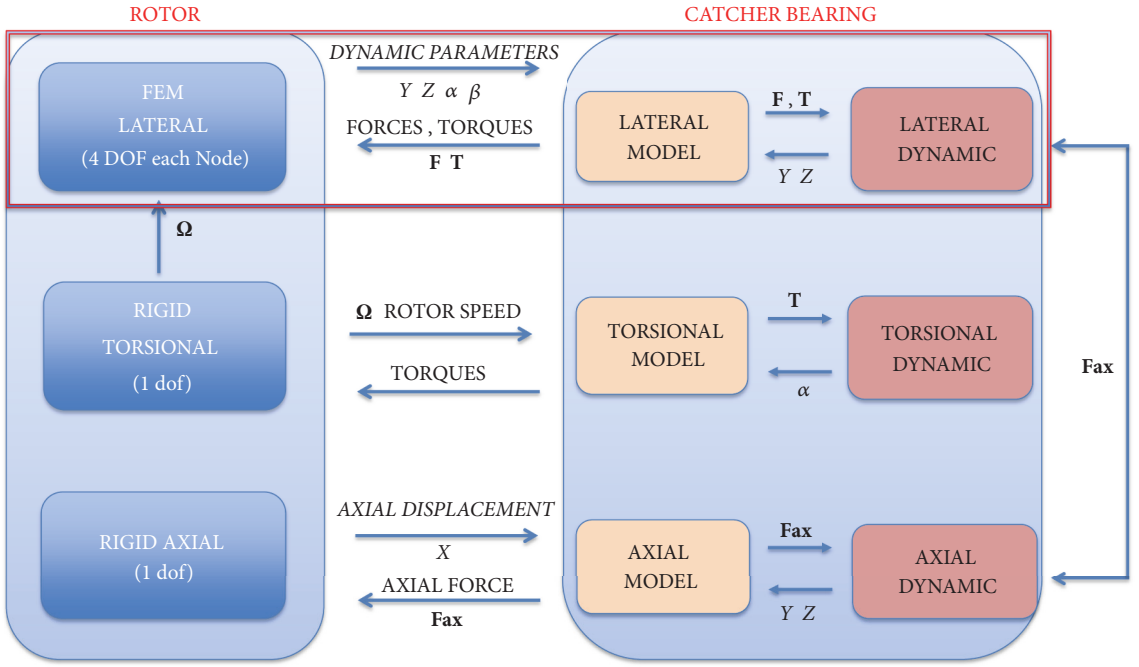

Figure 2: Model architecture.

acts on the outer race of the bearing, while the ribbon is placed between the outer ring of the auxiliary bearing and the housing; it creates both radial and tangential force components and has both elastic and damping characteristics. In the event of a full circular whirl mode, the ribbon characteristics greatly influence the frequency of the whirl motion.

The whole model is able to predict the behavior of the complete rotor-dynamic system during transient, steady and emergency conditions (e.g., emergency landing phenomena) and it is composed of two main submodels (see Figure 2):

(1) *Rotor model*, which includes a FEM model representing the lateral dynamics of the rotor and two simplified models, where the rotor is represented as a rigid body, to reproduce axial and torsional rotor dynamics; the main purpose is to have a good compromise between accuracy of the results and computational efficiency, considering the long time duration of the events to be simulated.

(2) *Auxiliary rolling bearing model*, characterized by a combination of multibody and contact models, able to represent the dynamics of the elements of the auxiliary system.

In order to reproduce the forward whirl phenomenon observed during combined radial-axial landing experimental tests, the lateral and the axial model have been coupled (see Figure 2): the axial force calculated in the rotor axial model represents an input for the catcher bearing lateral model.

The effect produced by this coupling allows well reproducing the phenomena observed during the experimental tests and, especially, the forward whirling.

2.2. Rotor Model. The lateral dynamic of the rotor is described by a FEM model, while the axial and the torsional dynamics are described by two simplified models (Figure 2) where the rotor is represented as a rigid body.

The kinematic quantities calculated by the rotor model (e.g., rotor nodes radial and axial displacements $\mathbf{y}$, $\mathbf{z}$, α, and β, rotor nodes velocities $\dot{\mathbf{y}}$, $\dot{\mathbf{z}}$, $\dot{\alpha}$, and $\dot{\beta}$, and rotor angular velocity $\boldsymbol{\Omega}$) represent the inputs of the auxiliary rolling bearing model; the interaction forces and moments (e.g., radial interaction forces between the rotor and the bearing F_r, interaction torques T, and axial forces $\mathbf{F_{ax}}$) between the bearing elements are calculated in the auxiliary bearing model and constitute the inputs of the rotor model. So, there is a reciprocal exchange of kinematic and dynamic quantities between the submodels at each time step of the simulation.

During the experimental tests carried out on a dedicated test rig, in particular during combined radial-axial landings, coupling effects between the lateral and the axial dynamics have been observed. Under an axial thrust load the experiments show a forward whirl rotor lateral orbit; in order to represent such effects, a specific coupled formulation between the two dynamic models has been developed.

The whole model provides a good representation of the dynamical behavior of the rotor with a low computational effort.

2.2.1. Rotor Lateral Model. In order to describe the lateral dynamics, the rotor is represented through a finite element discretization, where each rotor element is considered as a 2D BEAM (Figure 3). Such FEM model simulates the lateral rotor behavior, according to the classical rotor-dynamics equations of motion and accounting for magnetic and auxiliary bearings actions and external loads [20]; each BEAM element is

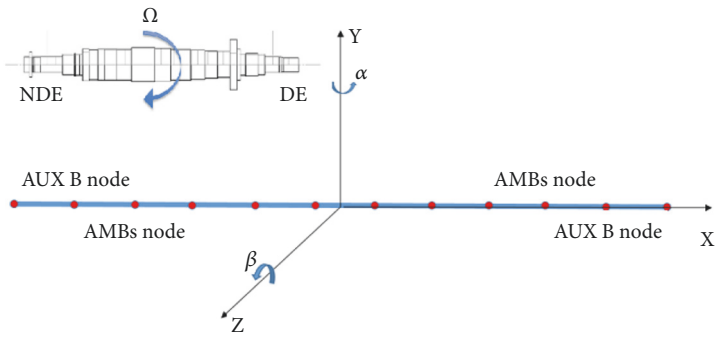

Figure 3: Discretization of the rotor in 2D BEAM elements.

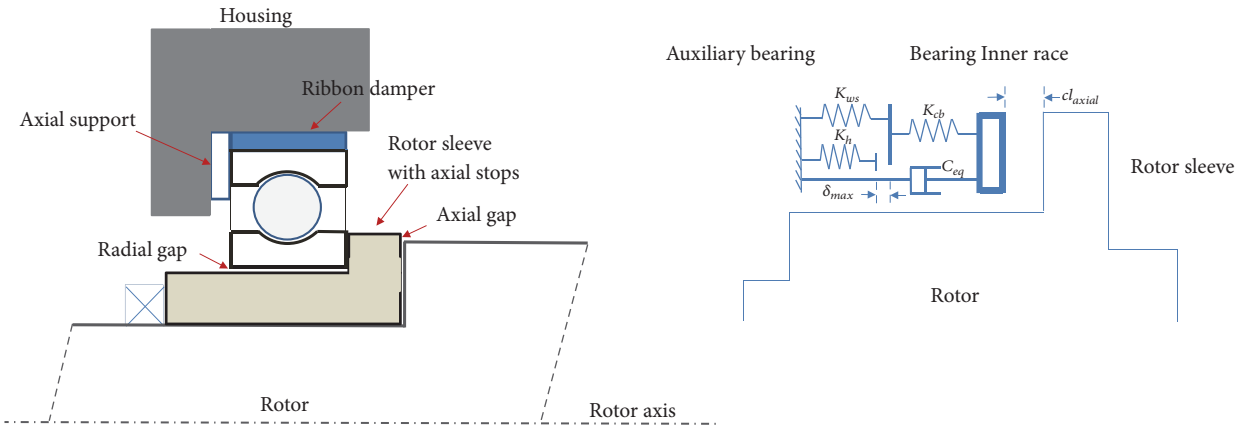

Figure 4: Schematic representation of the system axial model.

based on the Timoshenko Theory [20, 21]. Each node has 4 degrees of freedom: two radial translations and two rotations around the translational axes.

The inputs of the model are the forces and moments acting on the rotor in correspondence of the nodes where the magnetic and the auxiliary bearings are located and the external loads and torques (i.e., the unbalance load). The outputs of the rotor model are the kinematic quantities: positions $\mathbf{x}$ and velocities $\dot{\mathbf{x}}$ for each degree of freedom of the rotor nodes.

The equations of motion that represent the rotor lateral behavior are reported below [20]:

$$\mathbf{M_{rot}}\ddot{\mathbf{x}} + \mathbf{C_{rot}}\dot{\mathbf{x}} + \Omega\mathbf{G_{rot}}\dot{\mathbf{x}} + \mathbf{K_{rot}}\mathbf{x} = \mathbf{F}, \quad (1)$$

where $\mathbf{x}$ contains the two translational and the two rotational degrees of freedom of the rotor nodes (y, z, α, β), while $\mathbf{M_{rot}}$, $\mathbf{C_{rot}}$, $\mathbf{G_{rot}}$, and $\mathbf{K_{rot}}$ are, respectively, the mass, damping, stiffness, and gyroscopic matrices of the rotor; the vector F contains the external forces and moments acting on the rotor nodes.

Furthermore, a modal reduction for the rotor FEM lateral model has been implemented. The modal reduction used is based on the Craig-Bampton method and generates reduced rotor matrices (mass, stiffness, damping, and gyroscopic matrix) on the base of the number of nodes and modes chosen by the user to describe the considered system [22]; by using the modal reduction, it is possible to simulate long period of time in quite short simulation time, reaching a good compromise between results accuracy and computational efficiency.

2.2.2. Rotor Axial Model. In order to reproduce the axial rotor dynamics, a simple model has been developed in which the rotor is represented as a rigid body able to translate along its symmetry axis. The model describes the axial vibration of the rotor and the axial force, which are input for the lateral model and must be known at each instant of the simulation in order to have a real coupling between the lateral and the axial dynamics.

Figure 4 shows a scheme of the system axial model; the k_{ax}, c_{ax} parameters are the equivalent axial stiffness and damping of the system which have variable values depending on the rotor axial displacement; F_{thrust} is the thrust force applied by the actuator and is used to simulate the axial landing, while m_r is the rotor mass. In correspondence of the initial instant of the simulation, the rotor is placed at its initial position ($x_r(0) = 0$) where the axial clearance is equal to cl_{ax}; when the axial thrust force is applied to the system, the rotor moves according to the following dynamic equations:

$$\ddot{x}_r = -\frac{F_{thrust}}{m_r} + F_{ax}(t), \quad (2)$$

where F_{thrust} is the axial thrust force acting on the rotor and m_r is the rotor mass.

By knowing $x_r(t)$ and the equivalent stiffness k_{ax} and damping c_{ax} of the system (Figure 4), the axial reaction force F_{ax} can be calculated as

$$F_{ax}(t) = -k_{ax}x_r(t) - c_{ax}\dot{x}_r(t). \tag{3}$$

The axial force $F_{ax}(t)$ depends on the axial thrust load force F_{thrust} and acts on the lateral surface of the rotor sleeve and on the thrust surface of the inner race of the bearing. The axial contact between the rotor sleeve and the inner race of the rolling bearing produces a tangential force that is proportional to $F_{ax}(t)$ and the friction coefficient; for this reason, it acts on the lateral degrees of freedom of the rotor and of the bearing inner race and it represents the coupling between the lateral and the axial dynamic model: the axial force F_{ax}, calculated through (3), is the main input of the rotor lateral model and of the rolling bearing inner race lateral model.

The equivalent axial stiffness k_{ax} of the system can be calculated considering the stiffness elements (bearing stiffness k_{cb}, support stiffness k_{ws}, and housing stiffness k_h) and taking into account the axial displacement of the rotor: when the axial system displacement is less than the axial clearance, no stiffness is considered to work; as the system translation exceeds the axial clearance cl_{ax}, the support stiffness k_{ws}, and the bearing stiffness k_{cb} work together; so, before the axial displacement of the shaft reaches the value $\delta_m + cl_{ax}$ corresponding to the maximum deflection of the support, the equivalent axial stiffness can be obtained through the series of k_{cb} and k_{ws} and the axial force $F_{ax}(t)$ can be calculated as follows:

$$\begin{aligned}
&\text{if } |x_r| \le cl_{ax}\\
&F_{ax}(t) = 0\\
&\quad \text{if } x_r > cl_{ax} \;\&\; x_r \le cl_{ax} + \delta_m\\
&\qquad F_{ax} = -\left(\frac{1}{k_{cb}} + \frac{1}{k_{ws}}\right)^{-1}(x_r - cl_{ax}) - c_{ax}\dot{x}_r\\
&\quad \text{if } x_r < -cl_{ax} \;\&\; x_r \ge -(cl_{ax} + \delta_m)\\
&\qquad F_{ax} = -\left(\frac{1}{k_{cb}} + \frac{1}{k_{ws}}\right)^{-1}(x_r + cl_{ax}) - c_{ax}\dot{x}_r.
\end{aligned} \tag{4}$$

where x_r represents the axial coordinate of the rotor. When the axial displacement of the shaft exceeds the value $\delta_m + cl_{ax}$ (and the maximum deflection of the support is reached), the housing and the bearing stiffnesses k_h and k_{cb} work in series and the support stiffness k_{ws} does not play any role anymore:

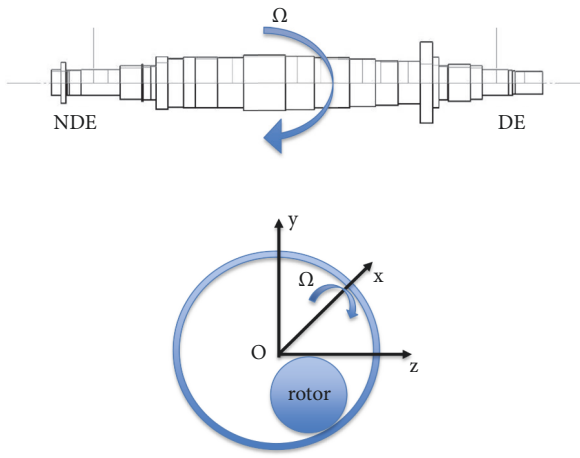

Figure 5: Scheme of the rotor motion.

$$\begin{aligned}
&\text{if } x_r > cl_{ax} + \delta_m\\
&\quad F_{ax} = -\left[\frac{1}{k_{cb}} + \frac{1}{k_h}\right]^{-1}[x_r - (cl_{ax} + \delta_m)]\\
&\qquad -\left(\frac{1}{k_{cb}} + \frac{1}{k_{ws}}\right)^{-1}\delta_m - c_{ax}\dot{x}_r\\
&\text{if } x_r < -(cl_{ax} + \delta_m)\\
&\quad F_{ax} = -\left[\frac{1}{k_{cb}} + \frac{1}{k_h}\right]^{-1}[x_r + (cl_{ax} + \delta_m)]\\
&\qquad +\left(\frac{1}{k_{cb}} + \frac{1}{k_{ws}}\right)^{-1}\delta_m - c_{ax}\dot{x}_r.
\end{aligned} \tag{5}$$

2.2.3. Rotor Spinning Model. In order to determine the rotor rotational velocity during the simulation, an approximate torsional model has been implemented, in which the rotor is described as a rigid body able to rotate around its symmetry axis. This simplified model allows obtaining a good representation of the torsional dynamics of the rotor, ensuring again a good compromise between accuracy and numerical efficiency.

The torques acting on the rotor are the auxiliary bearing moments and the windage torques (see (6)):

$$I\dot{\Omega} = \mathbf{T_{aux}} = \mathbf{T_{aux1}} + \mathbf{T_{aux2}} + \mathbf{T_{wind}}, \tag{6}$$

where I represents the torsional moment of inertia and $\dot{\Omega}$ is the rotor angular speed; T_{aux1} and T_{aux2} are the torques exerted by the two auxiliary bearings on the rotor while T_{wind} is the windage torque.

The rotor angular speed decreases, during a simulation, because of friction effects (see Figure 5).

2.3. Auxiliary Bearing Model. The catcher bearing model describes the dynamics of the bearing components and allows the calculation of the interaction forces and moments between their contact surfaces. By solving the equations of motion of each element of the auxiliary bearing system, it is

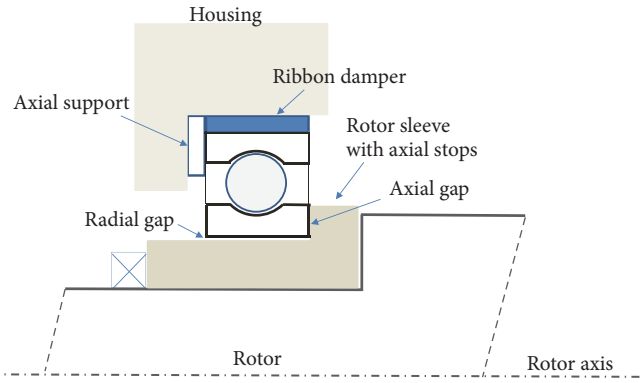

Figure 6: Schematic representation of the auxiliary system.

possible to calculate the position of the center of gravity of each element of the catcher bearing.

The catcher bearing system (diameter of the bearing equal to 60 mm) is shown in Figure 6 and is composed of the following elements:

(1) housing;

(2) ribbon damper;

(3) axial support;

(4) inner race;

(5) outer races;

(6) rolling elements;

(7) landing sleeve.

From a dynamical point of view, a simplifying assumption has been made: the catcher bearing elements are able to move in the plane, so the bearing inner race has 3 degrees of freedom (i.e., it can translate along the y and z directions and rotate around the x axis) while the outer race can only translate in the plane without rotating.

Equations (7) describe the translational dynamics of the rolling bearing inner race; the bearing inner race degrees of freedom are two because the inner race motion is considered to move in the radial plane of the bearing OYZ (Figure 5). This simplifying hypothesis allows obtaining a good compromise between the accuracy computational efficiency:

$$\begin{aligned} \mathbf{M_i}\ddot{\mathbf{x}}_\mathbf{i} + \mathbf{C_i}\dot{\mathbf{x}}_\mathbf{i} &= \mathbf{P} + \mathbf{F}, \\ \mathbf{F} &= \mathbf{F_{io}} + \mathbf{F_{ir}} + \mathbf{F_{rub}}, \end{aligned} \tag{7}$$

where $\mathbf{x_i}$ contains the coordinates of the inner race center of gravity, $\mathbf{M_i}$ is the inner race mass matrix, $\mathbf{C_i}$ is the inner race damping matrix, $\mathbf{P}$ is the weight force of the inner race, and the vector $\mathbf{F}$ is the sum of the radial forces acting on the bearing inner race (see also Figure 7): $\mathbf{F_{io}}$ is the interaction force on the inner race exerted by the rolling elements, $\mathbf{F_{ir}}$ is the contact force exchanged between the inner race and the rotor during the contact (including a normal $\mathbf{F_{rN}}$ component and a tangential one $\mathbf{F_{fr}}$; see (15)), and $\mathbf{F_{rub}}$ is the resultant force generated during the axial rub between the thrust surface of the bearing inner race and the lateral surface of the rotor sleeve (see (19)).

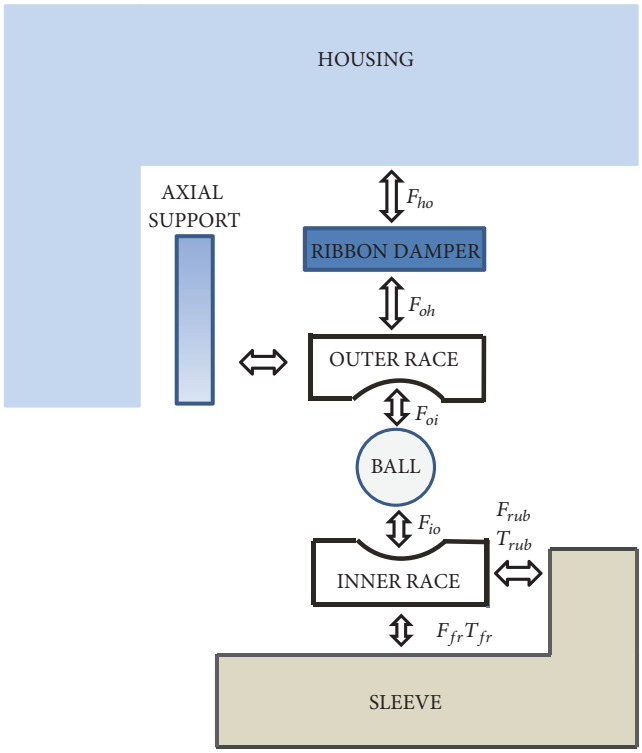

Figure 7: Schematic representation of the interactions between the elements of the auxiliary system.

Equation (8) describes the rotational dynamics of the bearing inner race:

$$I_i\dot{\Omega}_i = T_{fr} + T_{cb} + T_{rub} \tag{8}$$

where I_i is the torsional moment of inertia of the bearing inner race and T_{fr} is the moment acting on the inner race and due to the action of the radial friction force F_{fr}; T_{cb} is the ball bearing drag torque due to the rolling friction of the rolling elements during the motion and T_{rub} is the resultant torque due to the axial rub between the thrust surface of the bearing inner race and the lateral surface of the rotor sleeve.

The outer surface of the outer race interacts with the housing through the ribbon damper, which is an elastic-damping element; furthermore, there is another elastic element: the axial support on the outer race, placed between the external surface of the outer race and the statoric flange.

Equation (9) describes the translational dynamics of the bearing outer race, which can move into the radial plane OYZ (Figure 5):

$$\mathbf{M_o}\ddot{\mathbf{x}}_\mathbf{o} + \mathbf{C_o}\dot{\mathbf{x}}_\mathbf{o} = \mathbf{F_{oi}} + \mathbf{F_{oh}}, \tag{9}$$

where $\mathbf{x_o}$ contains the coordinates of the outer race center of gravity, $\mathbf{M_o}$ and $\mathbf{C_o}$ are the bearing outer race mass and damping matrices, the vector $\mathbf{F_{oi}}$ is the interaction force on the outer race exerted by the rolling elements, and $\mathbf{F_{oh}}$ is the radial force exchanged between the outer race and the housing flange.

The auxiliary bearings have spherical rolling elements, which have been modelled as force elements, without representing their dynamic behavior. The elastic force exerted by the rolling elements allows representing the interactions between the outer and the inner race of the bearings.

2.4. Contact Models. The catcher bearing model simulates the plane motion of the auxiliary bearing elements and calculates the possible interaction forces and moments among them; the kinematic physical quantities are determined by solving the equations of motion of each elements (see Section 2.3), while the interaction forces/moments are calculated through appropriate contact models based on the Hertz theory.

In this section, the contact models implemented in the proposed bearing model will be explained, showing the formulation used to calculate the interaction forces and moments between the contact surfaces.

The surfaces which interact during the motion are (see Figure 7):

(1) radial contact between the rotor landing sleeve and the inner surface of the bearing inner race: the contact force $\mathbf{F_{ir}}$ exchanged between the inner race and the rotor during the contact includes a normal $\mathbf{F_{rN}}$ component and a tangential one $\mathbf{F_{fr}}$; furthermore, a friction moment $\mathbf{T_{fr}}$ is generated;

(2) axial contact between the thrust surface of the rolling bearing inner race and the lateral side of the landing rotor sleeve: during axial or combined axial-radial rotor landings, axial rubbing force and moment are generated $\mathbf{F_{rub}}$, $\mathbf{T_{rub}}$;

(3) elastic interaction between the bearing outer race and the bearing inner race through the rolling elements: the balls exert an elastic force $\mathbf{F_{io}}$ on the inner race and $\mathbf{F_{oi}}$ on the outer races;

(4) the interaction force between the housing and the outer race is exerted through the ribbon damper element $\mathbf{F_{oh}}$.

2.4.1. Rotor-Inner Race Radial Interaction. Concerning the development of this part of the model, see also the paper [19]. During a radial landing, the inner surface of the bearing inner ring and the rotor landing sleeve get in contact; the rotor bounces, after the impact, on the inner ring and continues to rotate supported by the auxiliary bearings. As a result of the interaction with the rotor, the inner ring accelerates and tends to reach the rotor speed.

The contact forces $\mathbf{F_{rN}}$ exchanged between the rotor and the bearing inner ring is made up of two components: $\mathbf{F_{rN}}$ is the normal contact force and $\mathbf{F_{fr}}$ is the friction force due to the radial rubbing.

The mathematical steps required to calculate such forces are briefly reported below.

It is very useful to define a radial-tangential $(R(i_1), T(j_1))$ reference system and express the quantities of interest (e.g., bodies centers of gravity coordinates; velocities) in this specific system (Figure 8).

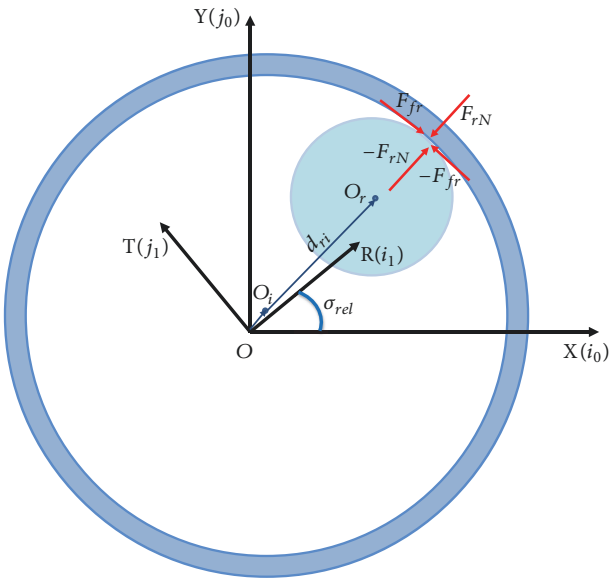

FIGURE 8: Interaction normal and friction forces between the rotor and the bearing inner ring.

Furthermore, it is convenient to refer the analysis to the relative displacements and velocities between the rotor and the inner race in radial and tangential coordinates. The relative displacements $\mathbf{d_{ri}}$ between the two bodies can be obtained from the difference between the coordinates of the rotor node $\mathbf{O_r}$ and the coordinates of the inner race center of gravity $\mathbf{O_i}$:

$$\mathbf{d_{ri}} = \mathbf{O_r} - \mathbf{O_i}. \tag{10}$$

Through the use of the relative coordinates, it is possible to define a relative angle of rotation σ_{rel} and, consequently, to determine the rotational matrix $\mathbf{R}$ needed to convert the quantities expressed in the Cartesian reference system $(Z(i_0), Y(j_0))$ into the radial-tangential reference system $(R(i_1), T(j_1))$.

Equation (11) defines the relative angle of rotation σ_{rel}:

$$\sigma_{rel} = \operatorname{atan} 2\left(y_{ri}, z_{ri}\right), \tag{11}$$

while (12) defines the transformation matrix $\mathbf{R}$:

$$R = \begin{bmatrix} \cos\left(\sigma_{rel}\right) & \sin\left(\sigma_{rel}\right) \\ \sin\left(\sigma_{rel}\right) & -\cos\left(\sigma_{rel}\right) \end{bmatrix}. \tag{12}$$

The relative displacements $\mathbf{d_{ri}}$ and velocities $\mathbf{v_{ri}}$ expressed in the Cartesian reference system can be expressed into the radial-tangential reference system using the rotational matrix $\mathbf{R}$:

$$\begin{aligned} \mathbf{d_{rt}} &= \mathbf{R}^T \mathbf{d_{ri}}, \\ \mathbf{v_{rt}} &= \mathbf{R}^T \mathbf{v_{ri}}. \end{aligned} \tag{13}$$

The contact forces and moments are calculated through the contact model if there is a interpenetration δ_{ri} between

the two bodies. By knowing the physical value of the radial clearance, the penetration between the two bodies along the radial direction can be calculated as follows:

$$\delta_{ri} = \left(y_{ri} - c_r\right). \tag{14}$$

Using the interpenetration δ_{ri}, it is possible to calculate the normal contact force $\mathbf{F_{rN}}$ and the friction force $\mathbf{F_{fr}}$ due to the radial rubbing between the rotor sleeve radial surface and the inner surface of the inner ring:

$$\begin{aligned} \mathbf{F_{rN}} &= \left(K_{hertz}\delta_{ri}^{\gamma} + K_{visc}\dot{\delta}_{ri}\delta_{ri}\right)\mathbf{i_1}, \\ \mathbf{F_{fr}} &= \mu_{rad}F_{rN}S\mathbf{j_1} \end{aligned} \tag{15}$$

where K_{hertz} is the Hertzian contact constant, K_{visc} is the viscous contact constant, μ_{rad} is the radial friction coefficient, and S is the sign function of the tangential component of the relative velocity v_t:

$$\mathbf{v_t} = v_{rt}\mathbf{j_1} + r_r\Omega_r\mathbf{k_1} - r_i\Omega_i\mathbf{k_1}. \tag{16}$$

The friction force $\mathbf{F_{fr}}$ due to the radial rubbing between the rotor sleeve and the inner ring generates a torque $\mathbf{T_{fr}}$ responsible for the acceleration of the inner race:

$$\mathbf{T_{fr}} = \frac{\left(r_i + r_r\right)}{2}F_{fr}\mathbf{k_1}. \tag{17}$$

During a pure radial landing, the rotor falls and bounces on to the inner ring of the bearing, which begins to rotate and quickly reaches the rotor angular speed; in case of high radial friction, the rotor performs a backward whirl orbit because of the friction effects between the rotor and the bearing inner ring.

On the other hand, during a combined axial-radial rotor landing due to AMBs failure (both radial and axial magnetic bearings), the rotor gets in contact with the inner surface of the inner ring and the thrust face of the catcher bearing. In case of high friction effects, a circular forward whirl rotor orbit has been observed in some experimental tests; in fact, as a consequence of repeated rotor landings, the bearing elements begin to be worn and the friction coefficient increases; the tangential actions due to that axial friction result to be stronger than the radial rubbing force.

2.4.2. Rotor Sleeve-Inner Race Axial Interaction. As regards the development of this part of the model, see also the paper [19]. Concerning the lateral dynamics, the rotor can perform small rotations around Y and Z axes; as a consequence of the rotor dynamics, the interpenetration between the lateral face of the rotor sleeve and the thrust surface of the inner ring cannot have a constant value; by knowing the inclination angles α and β of the rotor at any instant of time, it is possible to calculate the interpenetration value $\delta_{\mathbf{ri}}$ at each point of the thrust surface and, consequently, calculate the axial pressure P_{axial} at any point on the contact surface.

In order to calculate the resultant force and the resultant torque acting on the rotor due to the friction at the thrust surface, it is necessary to evaluate the relative slip velocity between the same point $A(r,\theta)$ on the rotor and on the bearing.

The vector $\dot{\mathbf{v}}_{\mathbf{A,r}}$ represents the velocity of the point $A(r,\theta)$ on the rotor, while the vector $\dot{\mathbf{v}}_{\mathbf{A,i}}$ represents the velocity of the point $A(r,\theta)$ on the bearing inner ring:

$$\begin{aligned} \mathbf{v_{A,r}}\left(r_A,\theta_A\right) &= \left[\dot{r}_r - \dot{\omega}_r r_A\sin\left(\theta_A\right)\right]\mathbf{i_1} + \dot{t}_r \\ &\quad - \dot{\omega}_r\left[r_{ri} - r_A\cos\left(\theta_A\right)\right]\mathbf{j_1}, \\ \mathbf{v_{A,i}}\left(r_A,\theta_A\right) &= \left[\dot{r}_i - \dot{\omega}_i r_A\sin\left(\theta_A\right)\right]\mathbf{i_1} + \dot{t}_i \\ &\quad - \dot{\omega}_i\left[r_A\cos\left(\theta_A\right)\right]\mathbf{j_1}. \end{aligned} \tag{18}$$

The relative velocity $\mathbf{v_{A,ri}}$ between the point A on the rotor and the same point A on the bearing can be simply calculated by subtracting the inner ring velocity $\mathbf{v_{A,r}}$ from the rotor velocity $\mathbf{v_{A,i}}$.

By knowing the relative velocity between the rotor and the bearing, the resultant force $\mathbf{F_{rub}}$, acting on the rotor and due to friction at the contact interface, can be evaluated by integrating the pressure field over the contact area:

$$\mathbf{F_{rub,r}} = -\mu_{ax}\int_{r_1}^{r_2}\int_0^{2\pi}\frac{P_{A,r}\left(\dot{r}_r\mathbf{i_1} + \dot{t}_r\mathbf{j_1}\right)}{\left\|\mathbf{v_{A,ri}}\right\|}r_A d\theta_A dR_A, \tag{19}$$

where μ_{ax} is the friction coefficient between the lateral face of the rotor sleeve and the thrust face of the bearing.

The torque due to the axial contact between the rotor and the bearing inner race can be determined as follows:

$$\begin{aligned} &\mathbf{T_{rub,r}} \\ &= -\mu_{ax}\int_{r_1}^{r_2}\int_0^{2\pi}\frac{P_{A,r}\left(\dot{t}_r\cos\left(\theta_A\right) + \dot{r}_r\sin\left(\theta_A\right)\right)}{\left\|\mathbf{v_{A,ri}}\right\|}r_A^2 d\theta_A dR_A\mathbf{k_1}. \end{aligned} \tag{20}$$

The torque on the rotor and on the bearing is considered to be equal and opposite:

$$\mathbf{T_{rub,r}} = -\mathbf{T_{rub,i}}. \tag{21}$$

2.4.3. Outer Race-Inner Race Radial Interaction. The interaction force $\mathbf{F_{io}}$ between the bearing inner and outer races is the radial reaction due to the relative motion of the races.

The races can interact through the rolling elements, which are modelled as force elements; through the load-deflection curve of the catcher bearing it is possible to extrapolate the stiffness characteristics of the rolling elements (k_{b1} and k_{b2}) and define the interaction force $\mathbf{F_{io}}$ with a second order polynomial function:

$$\mathbf{F_{io}} = \left(k_{b2}r_{io}^2 + k_{b1}r_{io}\right)\mathbf{i_1}, \tag{22}$$

where r_{io} is the relative displacement between the inner and the outer races centers of gravity.

The rolling elements exert also another important action on the catcher bearing: the rolling friction due to the balls generates a drag torque onto the inner ring, which decelerates under this effect. The approach to calculate the resistant torque $\mathbf{T_{CB}}$ is based on the Harris-Palmgren formulation [23], but, instead of considering the applied static load, the

dynamic radial and axial forces acting on the bearing have been taken into account:

$$\mathbf{T_{CB}} = f_1 F_\beta d_m \mathbf{k_1}, \tag{23}$$

where f_1 is a factor depending on the bearing design and relative bearing load, F_β depends on the magnitude and direction of the applied load, and d_m is the pitch diameter of the bearing.

For a ball bearing, Harris [23] defines f_1 as

$$f_1 = z\frac{F_s^y}{C_s}, \tag{24}$$

where F_s represents the equivalent dynamic load and C_s is the basic static load rating usually provided in the manufacturer catalog, while z and y represent empirical coefficients.

For a single row angular contact bearing the equivalent load $\mathbf{F_s}$ can be defined as follows:

$$F_s = X_s F_{radial} + Y_s F_{ax}, \tag{25}$$

where $X_s = 0.5$ and Y_s varies with the bearing contact angle α:

$$Y_s = c_1\alpha^2 + c_2\alpha + c_3. \tag{26}$$

For a radial ball bearing F_β is given by

$$F_\beta = c_4 F_{ax}\cot(\alpha) + c_5 F_{radial}. \tag{27}$$

The numeric parameters c_1, c_2, c_3, c_4, and c_5 of (26) and (27) have been determined on the base of the bearing geometry and characteristics: $c_1 = 7.142910^{-5}$, $c_2 = -1.244310^{-2}$, $c_3 = 0.64129$, $c_4 = 0.9$, and $c_5 = -0.1$.

2.4.4. Outer Race-Housing Interaction. The ribbon damper is located between the bearing outer ring and the housing; it has both elastic and damping characteristics (i.e., structural and viscous damping) and generates radial and tangential force components. The characteristics of the ribbon greatly influence the frequency of the rotor whirl motion.

The interaction force between the outer race and the housing $\mathbf{F_{oh}}$ can be expressed through the force exerted by the ribbon:

$$\mathbf{F_{oh}} = -C_{rib}\dot{\mathbf{x}}_\mathbf{o} - K_{rib}\mathbf{Q}\mathbf{x}_\mathbf{o} - K_{rib}\mathbf{I}\mathbf{x}_\mathbf{o}, \tag{28}$$

where $\mathbf{I}$ is the identity matrix, $\mathbf{x_o}$ is the vector of the coordinates of the outer race center of gravity, C_{rib} is the ribbon viscous damping, $K_{rib} = 6.3 * 10^7$ N/m is the ribbon stiffness, and $\mathbf{Q}$ is a matrix defined as follows:

$$Q = \begin{bmatrix} 0 & -\eta S_v \\ \eta S_v & 0 \end{bmatrix}. \tag{29}$$

The parameter η is a cross coupled stiffness factor, while S_v is the sign of the relative tangential velocity between the outer bearing and the housing.

For combined axial-radial rotor landings, because of the axial thrust force applied to the bearing inner race, a reaction force exerted by the housing on the outer race through the axial support is present. The force contribution due to this interaction is the damping force $\mathbf{F_{oh}}$:

$$\mathbf{F_{oh}} = -\frac{F_{ax}\mu_d}{\|\dot{\mathbf{x}}_\mathbf{o}\|}\dot{\mathbf{x}}_\mathbf{o}, \tag{30}$$

where μ_d is the Coulomb friction coefficient between the outer race and the housing and must be added to (28).

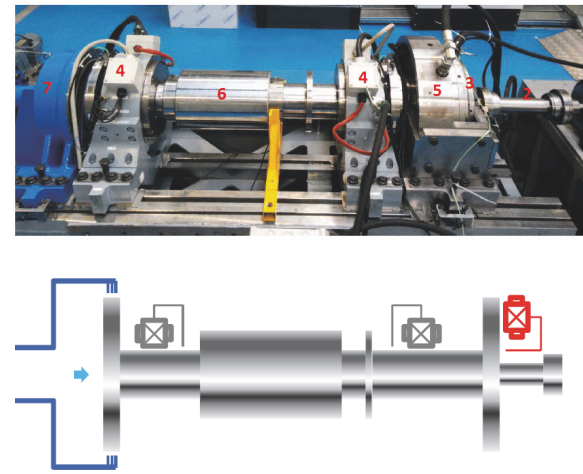

Figure 9: Experimental apparatus; from left to right: axial actuator, NDE radial magnetic bearing, speed sensor, DE radial magnetic bearing, magnetic thrust bearing, and power transmission coupling.

2.5. Test Rig Architecture. Figure 9 shows an overview of the scaled test rig considered for the development and the validation of the proposed model. The main components of the test rig are highlighted in the following:

(1) electric motor (1);

(2) power transmission coupling (2);

(3) force sensor (3);

(4) radial AMBs and auxiliary bearing (4); they are concentric;

(5) axial centering AMB (5);

(6) rotor (6);

(7) axial actuator (7).

Figure 10 shows a scheme of the test rig that is equipped with a sensors system able to estimate components temperature, forces, acceleration, vibrations, and speeds:

(1) load cells (*LC*);

(2) proximity sensors (*PS*);

(3) encoders (*EN*);

(4) accelerometers (*A*);

(5) thermocouples (*TC*).

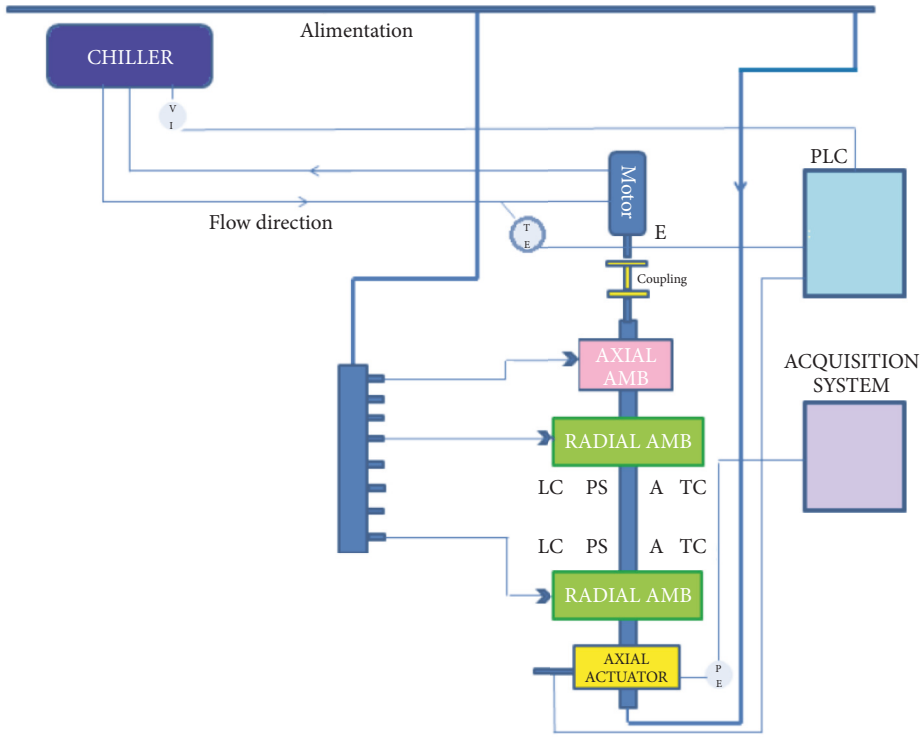

Figure 10: Scheme of the experimental apparatus.

The tests performed on the test rig allow the identification of the system behavior in landing conditions. In particular the tests carried out on the test rig belong to three different types (with different rotor speeds): radial landings (deactivating just radial AMBs), axial landings (deactivating just axial AMB), and combined radial-axial landings (deactivating both the AMBs).

The experimental tests taken as a reference in this paper for the model validation (Section 3) are no whirling rotor radial landing, a pure radial landing characterized by a normal friction condition; whirling rotor radial landing, a pure radial landing with high friction coefficient; whirling rotor combining axial-radial landing with high axial thrust force value.

3. Results

The proposed model allows performing the simulation for all the classical operating conditions and to set up parameters like the rotor angular velocity, the friction coefficients, and the landing time.

In this section the most interesting results of the main simulations are reported and compared to the related experimental results. In particular, it is easy to observe the different dynamic behavior of the rotor in case of radial landing (with normal friction conditions and high friction conditions) and of combined axial-radial landing. During a pure radial landing characterized by normal friction conditions, the rotor bounces on to the bearing inner rings and, after the first bounces, the rotor and the inner ring rotate at the same angular speed. In case of a pure radial landing characterized by high radial friction coefficient, the rotor realizes a backward orbit; while in a combined axial-radial landing with a high axial thrust force value acting on the rotor, the tangential forces generated in the axial contact cause a rotor forward whirl. The backward and forward whirl phenomena occur in particular conditions of high axial or radial friction; in fact, after a sequence of radial or combined axial-radial landings, some bearing elements begin to be worn (e.g., bearing inner race) as a consequence of the high impact and friction forces and consequently, the friction coefficient increases causing the whirling phenomenon.

All the simulation results reported in the paper have been obtained by using both variable step ODE algorithms and fixed step ODE algorithms [24]. The choice of the constant step for the fixed step algorithms and of the maximum step size for the variable step algorithms (together with the related tolerances) has been made to have a characteristic integration frequency (i.e., the inverse of the time step) always greater than the most significant frequencies of the considered system.

3.1. No Whirling Landing. In case of overloads or failure of the energy supply, the AMBs are disabled and the rotor falls and impacts on the inner rings of the auxiliary bearings.

The reported results show the displacements, forces, and orbits of specific rotor nodes; in particular, the nodes where the auxiliary bearings are located at the drive end and at the

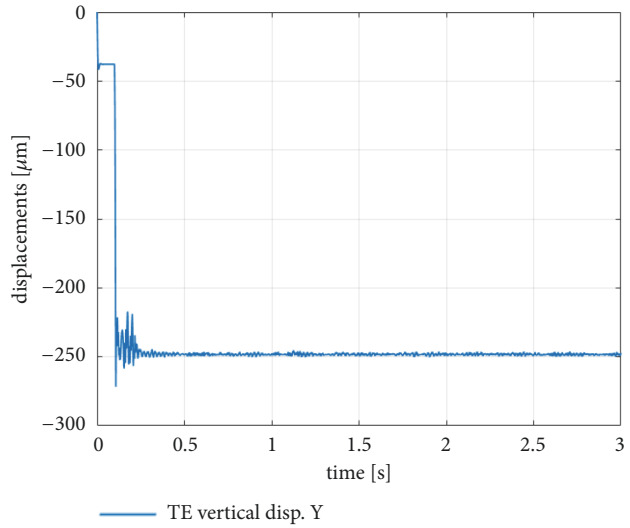

Figure 11: Predicted rotor vertical displacements during a landing test (DE node).

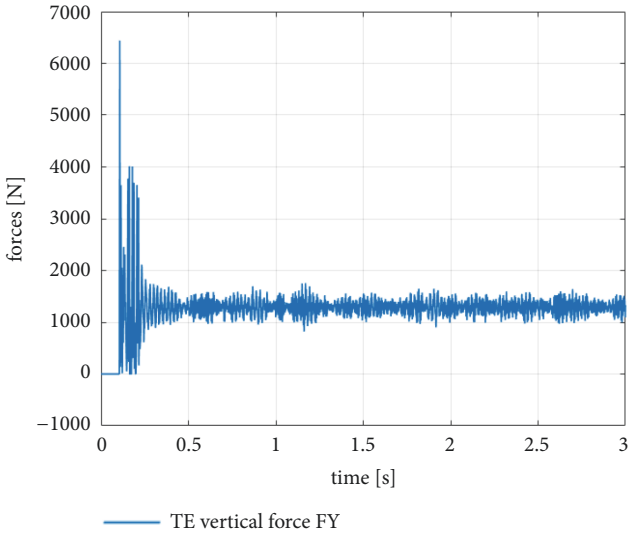

Figure 12: Predicted rotor vertical forces during a landing test (DE node).

nondrive end of the machine (for brevity denoted DE node and NDE node) have been considered.

The reported simulation and experimental test reproduces a rotor landing, in which the rotor has an angular speed equal to 7000 RPM and the AMBS are deactivated; so, as a consequence, the rotor lands on the auxiliary bearing system bouncing on to the bearing inner rings. During this first radial landing test (low radial friction without backward whirling), the following values were set for the speed Ω, the radial friction μ_{rad}, the axial friction μ_{ax}, and the axial load F_{thrust}: Ω =7000rpm, μ_{rad} =0.15 (low radial friction), μ_{ax} =0.3, and F_{thrust} =0N (no axial load).

In Figures 11 and 14 it is possible to observe the vertical and the horizontal displacements of the DE rotor node; by comparing the simulated plots with the experimental displacements reported in Figures 13 and 16, it is possible

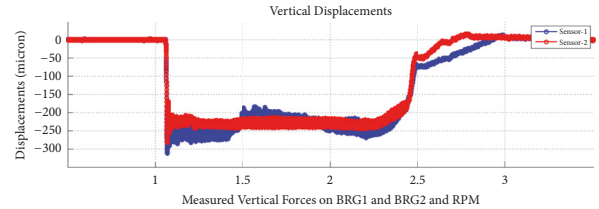

Figure 13: Experimental rotor vertical displacements during a landing test at DE (blue line) and NDE (red line) rotor nodes.

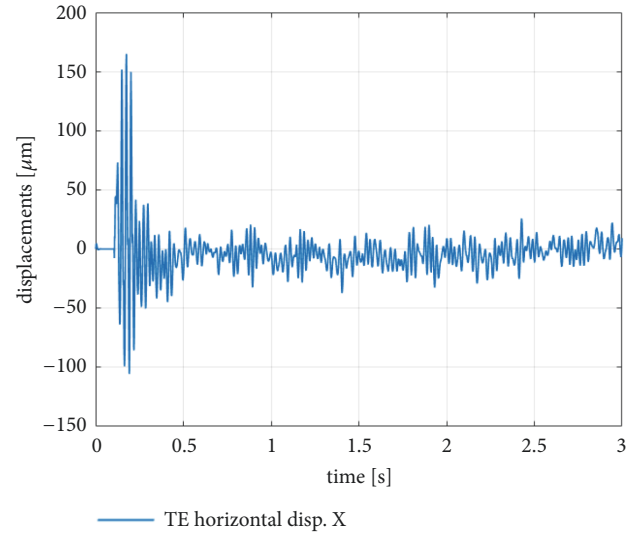

Figure 14: Predicted rotor horizontal displacements during a landing test (DE node).

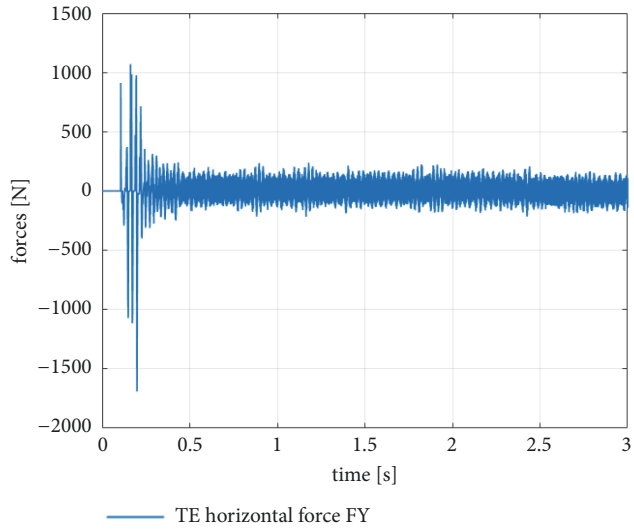

Figure 15: Predicted rotor horizontal forces during a landing test (DE node).

to note a good representation of dynamic rotor behavior. The vertical displacements show some initial peak values, which correspond to the first rotor bounces on the inner rings characterized by a high energy content; after that, the rotor and the bearing inner ring rotates at the same angular speed. In Figures 12 and 15 the vertical and the horizontal forces

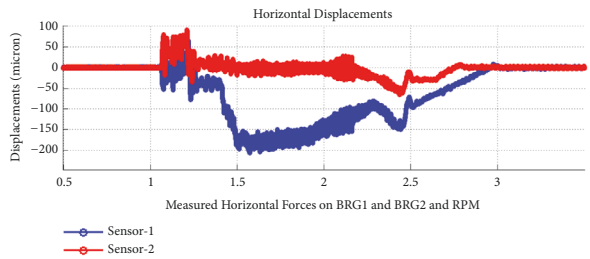

Figure 16: Experimental rotor horizontal displacements during a landing test at DE (blue line) and NDE (red line) rotor nodes.

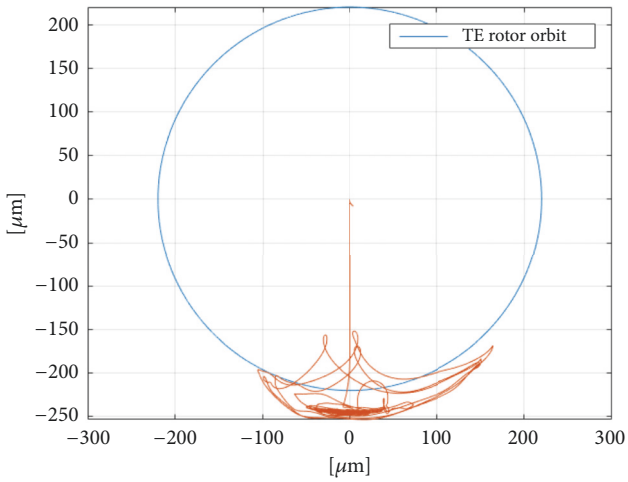

Figure 17: Predicted rotor orbit during a landing test (DE node).

acting on DE node show peak values in correspondence of the first rotor bounces.

Figure 17 shows the orbit described by the DE rotor node during the simulation; the blue circle is the nominal gap between the landing bearing bore and the landing sleeve, while in Figure 18 the experimental rotor orbit is reported.

3.2. Whirling Radial Landing. During a radial landing the rotor falls and impacts on the inner ring of the auxiliary bearing, it bounces on the ring, and in case of high friction and any conditions of wear, after some second tenths the rotor begins to whirl; in case of radial landing the contact force between the rotor sleeve and the inner ring of the bearing causes a backward whirl rotor orbit (Figure 27), considering the rotor angular speed convention shown in Figure 19. The reported results show the displacements, forces, and orbits of specific rotor nodes; in particular, the nodes where the auxiliary bearings are located at the drive end and at the nondrive end of the machine (for brevity denoted DE node and NDE node) have been considered. The rotor backward whirl is the predominant phenomenon in case of pure radial landings because of the radial friction effects.

The reference simulation reproduces a pure radial landing where the rotor rotates with an angular speed equal to 7000 RPM, the AMBS are deactivated, and the rotor lands on the auxiliary bearing system; between the inner race of the

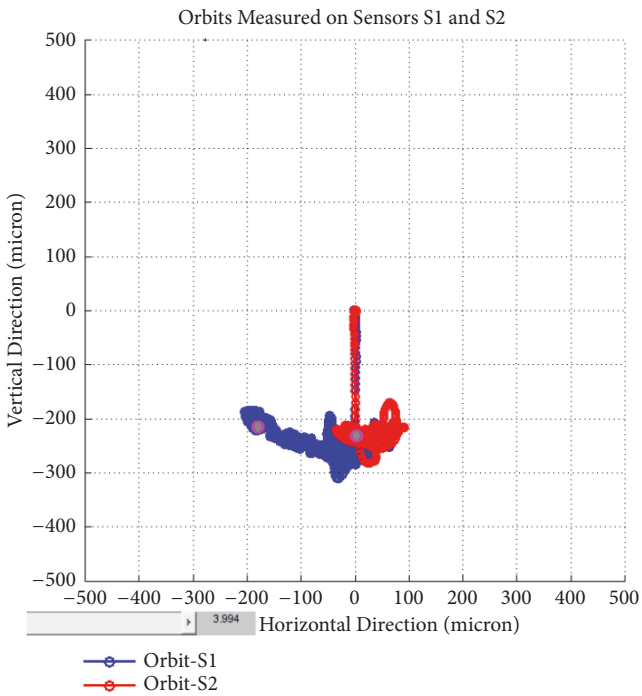

Figure 18: Experimental rotor orbit during a landing test.

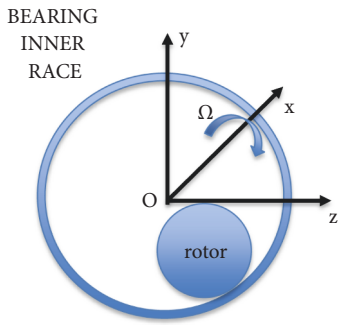

Figure 19: Rotor angular speed convention: rotor positive angular speed is clockwise.

catcher bearing and the rotor landing sleeve surface, friction radial forces arise: such forces are responsible for the rotor backward whirl orbit.

In order to emphasize such behavior, the radial friction coefficient has been set to a quite high value with respect to the combined axial-radial landings, where the axial friction coefficient is predominant on the radial one. The high value of the friction coefficient simulates the wear condition of the bearing elements due to the repeated landings.

During this second radial landing test (high radial friction with backward whirling), the following values were set for the speed Ω, the radial friction μ_{rad}, the axial friction μ_{ax}, and the axial load F_{thrust}: Ω =7000rpm, μ_{rad} =0.3 (high radial friction), μ_{ax} =0.3, and F_{thrust} =0N (no axial load).

In Figures 20 and 24 it is possible to observe the vertical and the horizontal displacements of the DE rotor node (the time zooms of such quantities are reported in Figure 21

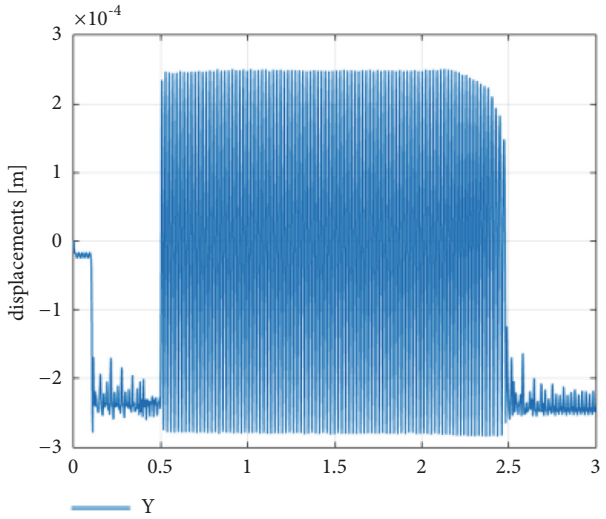

Figure 20: Predicted rotor vertical displacements during a radial landing test (DE node).

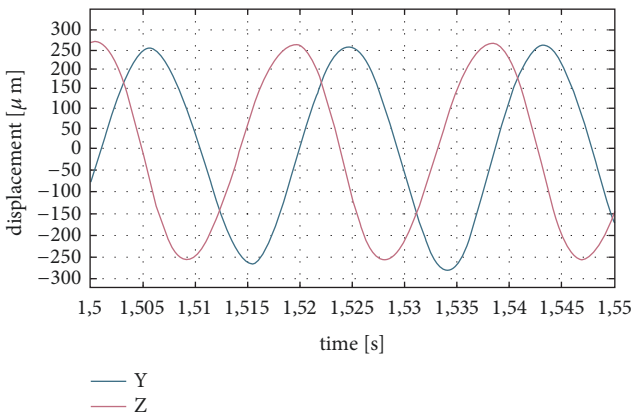

Figure 21: Time zoom of the predicted rotor vertical (in blue) and horizontal (in red) displacements during a radial landing test (DE node).

to better highlight amplitudes, phases and frequencies). By comparing the simulated plots with the experimental displacements reported in Figures 23 and 26, it is possible to note a good representation of the backward rotor orbit. The vertical displacements show some initial peak values, which represent the rotor bounces on the inner ring; after 0,5 s the vertical displacements switch from maximum negative values to maximum positive values: such oscillatory trend produces the backward whirl rotor orbit. Figure 27 show the orbits described by the DE rotor node during the simulation; the blue circle represents the nominal gap between the landing bearing bore and the landing sleeve. In Figures 22 and 25 the vertical and the horizontal forces on the rotor node in correspondence of the auxiliary bearing located at the DE side of the machine are reported; it is possible to observe the high dynamical values of such forces during the backward whirl.

In Table 1 the comparison between some significant results of the experimental tests and the related numerical

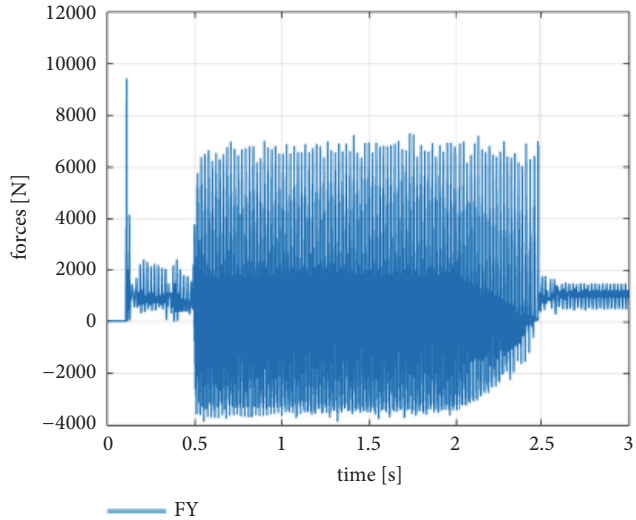

Figure 22: Predicted rotor vertical forces during a radial landing test (DE node).

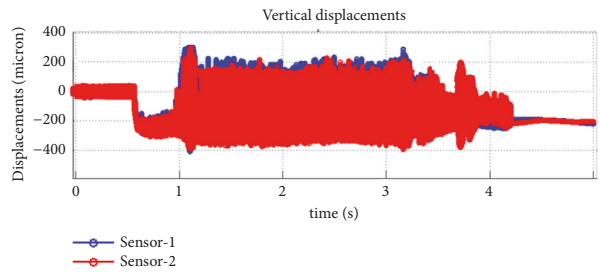

Figure 23: Rotor vertical displacements during a radial landing experimental test at DE (blu line) and NDE (red line) rotor nodes.

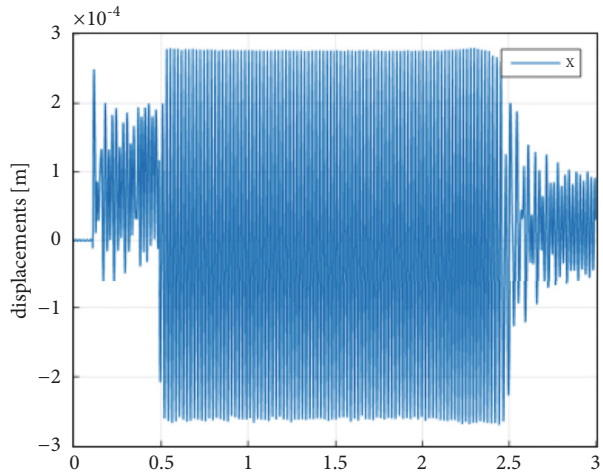

Figure 24: Predicted rotor horizontal displacements during a radial landing test (DE node).

simulations is reported: there is a good alignment between the displacements, and the activation time of the backward whirl has the same values.

3.3. Whirling Combined Axial-Radial Landing. In this section the most significant results of the axial-radial combined

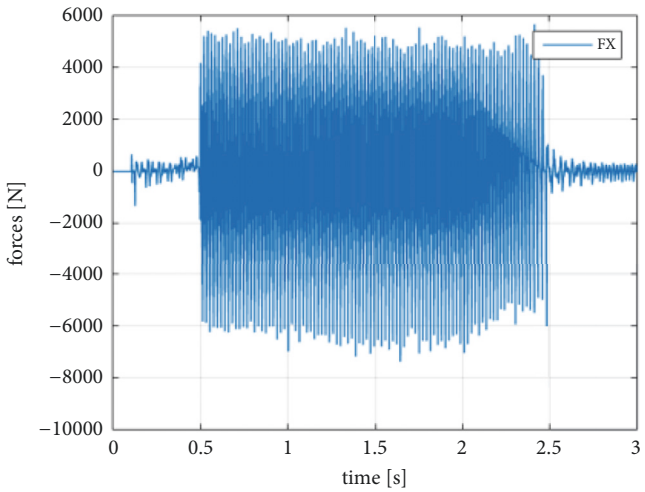

Figure 25: Predicted rotor horizontal forces during a radial landing test (DE node).

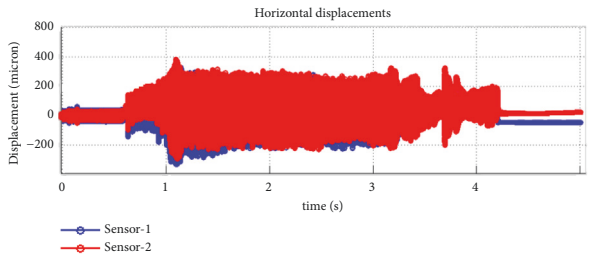

Figure 26: Rotor horizontal displacements during a radial landing experimental test at DE (blue line) and NDE (red line) rotor nodes.

Table 1: Radial landing results comparison.

Simulated		Experimental	
V.Disp.[mm]	Act.Time[s]	V. Disp.[mm]	Act.Time[s]
0.25 -0.28	0.4	0.2 -0.4	0.4
Backw. Freq. [Hz]			Backw. Freq. [Hz]
51			49

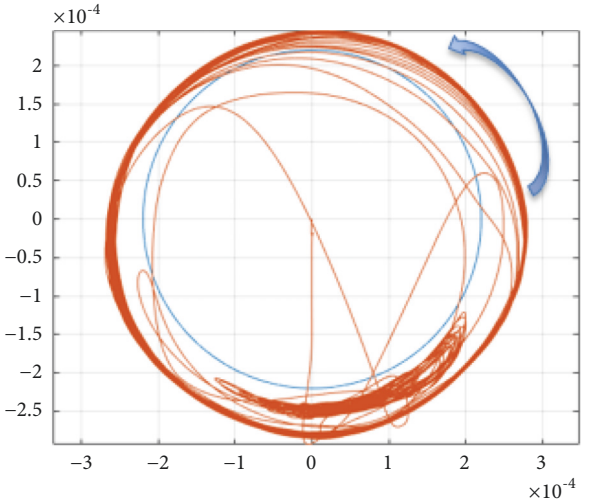

Figure 27: Predicted rotor backward whirl orbit at the DE rotor nodes.

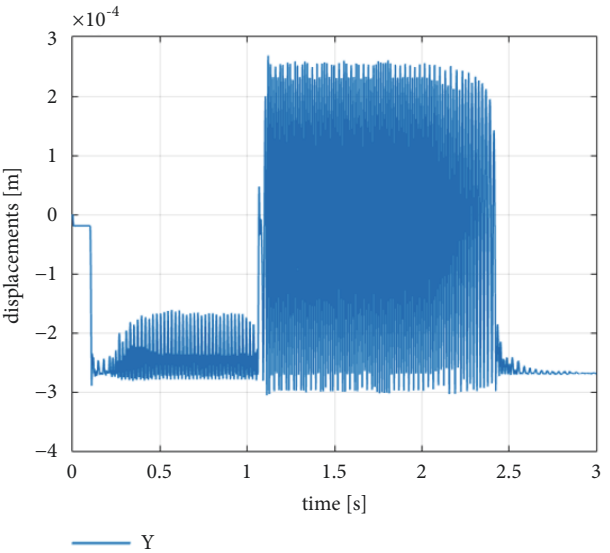

Figure 28: Predicted rotor vertical displacements at DE node during a combined landing test.

landing have been reported. The results reported in this paper are aimed at highlighting the forward whirl, the most important phenomenon observed during the combined landings; it occurs when the tangential forces between the lateral surface of the inner ring and the thrust surface of the rotor sleeve, caused by the axial friction, have a high value. In this condition such tangential forces prevail on the radial friction effects, which are responsible for the rotor backward whirl, and the forward whirl may occur. As in the previous case, the forward whirl is a particular phenomenon which may take place in case of high friction and wear conditions.

The considered simulation corresponds to a test in which the rotor rotates with an angular speed equal to 7000 RPM supported by the AMBs; the AMBs are deactivated, the rotor falls, and lands on to the auxiliary bearings. At the same time also the axial AMB is deactivated and an axial thrust force acts on the system determining the axial displacement of the rotor and the contact between the inner race and the landing sleeve.

In case of a combined radial-axial landing the rotor performs a forward whirl orbit: in fact, during the axial landing the thrust surface of the inner ring gets in contact with the lateral surface of the rotor sleeve; because of this interaction, friction tangential forces are generated and the rotor begins to perform a forward whirl orbit. During the axial-radial landing test (with forward whirling), the following values were set for the speed Ω, the radial friction μ_{rad}, the axial friction μ_{ax}, and the axial load F_{thrust}: Ω =7000rpm, μ_{rad} =0.15 (low radial friction), μ_{ax} =0.3, and F_{thrust} =4000N.

In Figures 28, 30, 31, and 32 it is possible to observe vertical and horizontal displacements and the corresponding

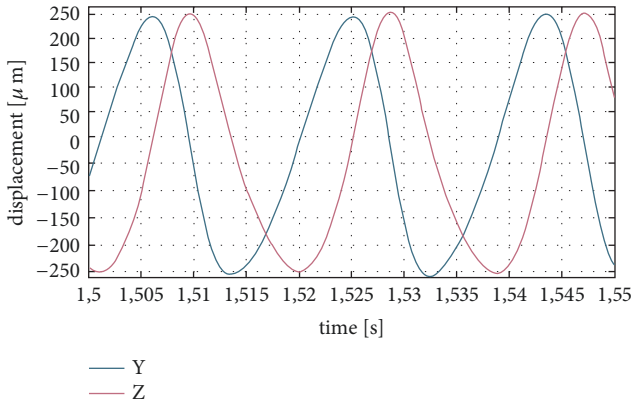

Figure 29: Time zoom of the predicted rotor vertical (in blue) and horizontal (in red) displacements at DE node during a combined landing test.

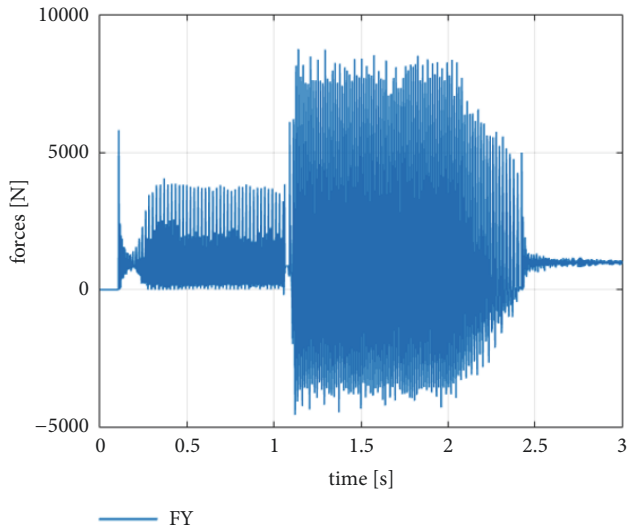

Figure 30: Predicted rotor vertical forces at DE node during a combined landing test.

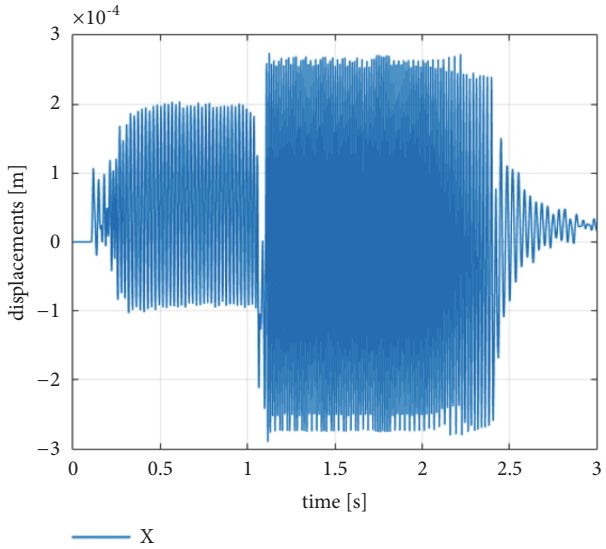

Figure 31: Predicted rotor horizontal displacements at DE node during a combined landing test.

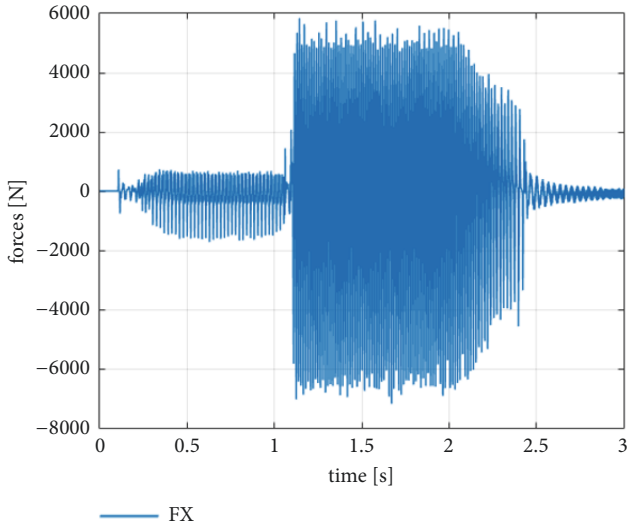

Figure 32: Predicted rotor horizontal forces at DE node during a combined landing test.

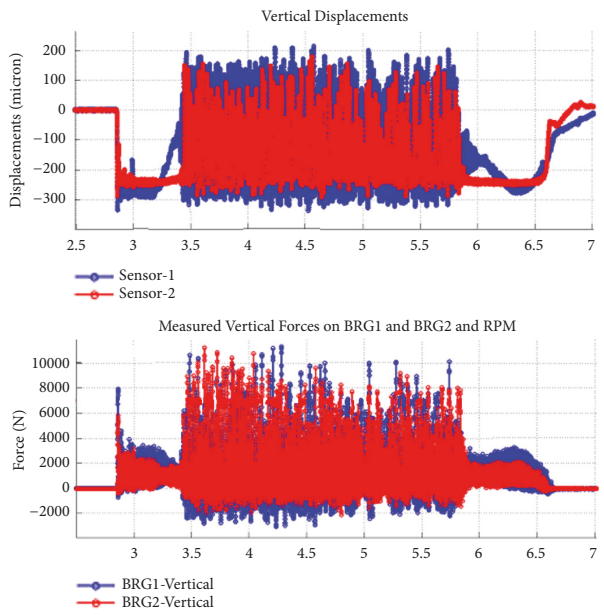

Figure 33: Experimental vertical displacements and forces at DE (blue line) and NDE (red line) rotor nodes.

force trends during the whole simulation. The time zooms of vertical and horizontal displacements of the DE rotor node are reported in Figure 29 to better highlight amplitudes, phases, and frequencies. Figures 33 and 34 show the results obtained from the experimental test corresponding to the simulation of the combined landing.

By making a comparison between the resultant vertical displacements and forces of the simulation and the experimental results, it is possible to find a good agreement between experimental and numerical physical quantities.

The orbits of the DE and NDE rotor nodes resulting from the numerical simulation are a bit different from the experimental orbits: in the experimental test the rotor begins

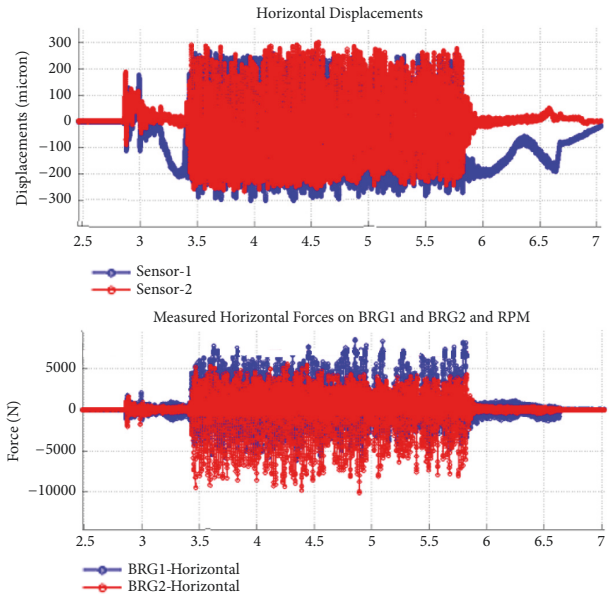

Figure 34: Experimental horizontal displacements and forces at DE (blu line) and NDE (red line) rotor nodes.

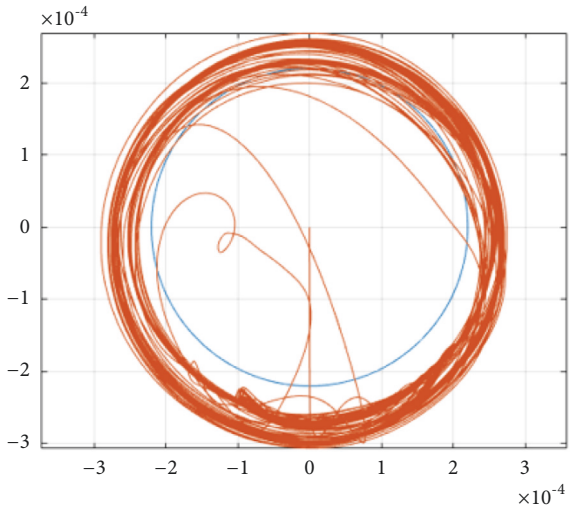

Figure 35: Predicted rotor DE node orbit.

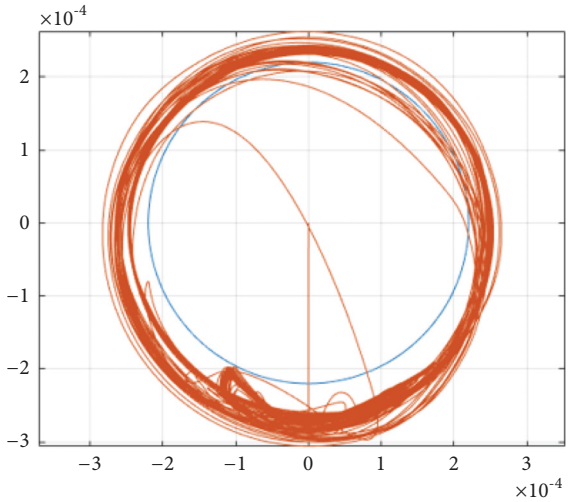

Figure 36: Predicted rotor NDE node orbit.

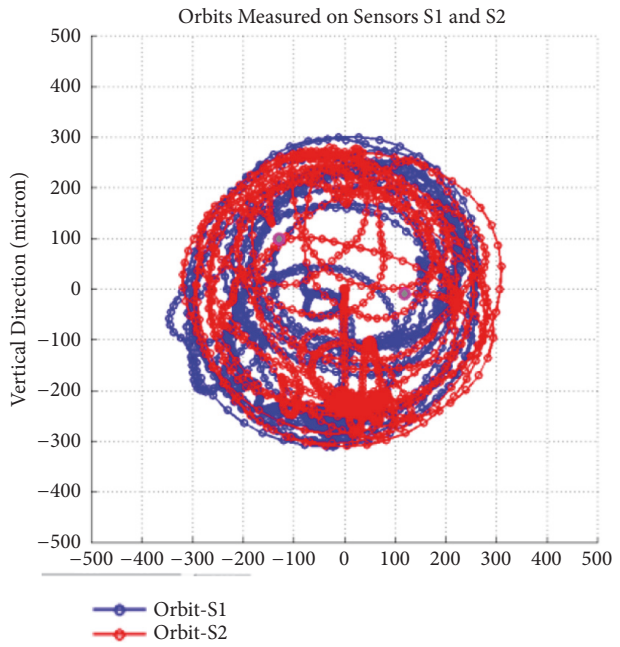

Figure 37: Experimental rotor orbit of the DE node (blue line) and NDE node (red line) rotor nodes.

to whirl slower and the orbits are fuller as a consequence of the whirling dynamics observed on the test rig: the whirling activation and deactivation on the real test are slower compared to the results obtained through the numerical simulation (see Figures 35, 36, and 37).

In order to extrapolate the frequency content of the vertical displacement of the DE rotor node signal, the Fourier Transform Method has been applied; through this method the signal has been described in the frequency domain to identify the characteristic forward whirl frequency (Figure 38).

In Table 2, the comparison between some numerical results of the simulation and the experimental data obtained from the experimental tests is reported for a combined axial-radial landing: there is a good alignment between

Table 2: Combined landing results comparison.

Simulated		Experimental	
V.Disp. [mm]	V.Forces [KN]	V. Disp. [mm]	V.Forces [KN]
0.2 -0.28	4.5 -1.5	0.15 -0.3	4.5 -0.5
Forw. Freq. [Hz]			Forw. Freq. [Hz]
50			48
67			65
80			77

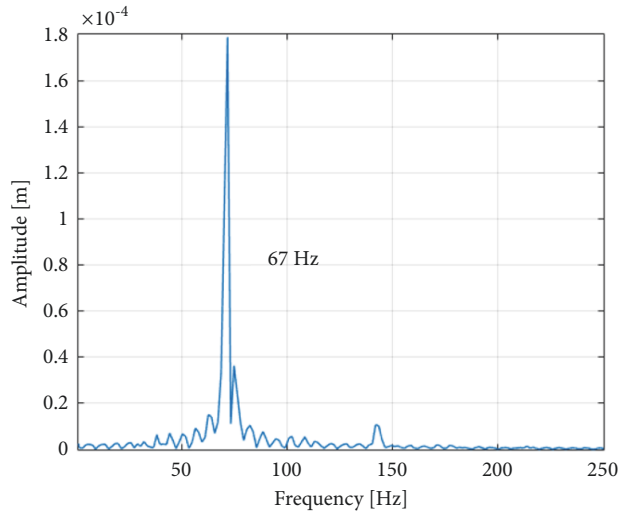

Figure 38: Simulated whirling frequency (rotor angular speed 7000 RPM).

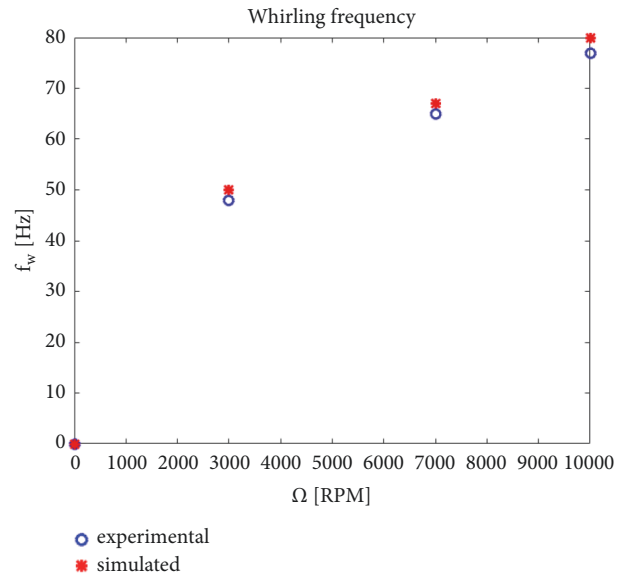

Figure 39: Comparison between experimental and simulated forward whirl frequency.

the dynamic forces and the related vertical displacements. Furthermore, the forward whirl frequencies, reported for three different speeds Ω =3000rpm - 7000 rpm - 10000 rpm, are well reproduced (see Figure 39).

4. Conclusions

The model presented in this paper is able to predict the behavior of a complete auxiliary bearing system under transient, steady, and emergency conditions (e.g., delevitation and landing phenomena) and it is composed of different submodels: the rotor submodel, which includes a FEM model to describe the lateral dynamics of the rotor and two rigid body models to reproduce axial and torsional rotor dynamics, and the auxiliary rolling bearing submodel, characterized by a combination of multibody and contact models able to describe the dynamics and the interactions of the auxiliary system components.

The model is able to reproduce the key effects observed during the experimental tests and, in particular, the forward whirl phenomenon. In order to carefully study some special phenomena like rotor landings, which require long period of time to evolve and involve many bodies and degrees of freedom, or other particular events like impacts, which occur in a short period of time, a compromise between accuracy and numerical efficiency has been pursued.

To validate the model, experimental tests have been performed on a scaled test rig in collaboration with Baker Hughes a GE company. A radial and a combined axial-radial landing of the rotor on the auxiliary bearings under specific operating conditions have been taken as reference in order to validate the numerical model. The physical and the contact parameters have been correctly set thanks to the many experimental data.

The results of the simulations well match the data coming from the experimental tests, confirming the reliability of the model and its robustness against the uncertainties affecting the system parameters.

Furthermore, thanks to the model modularity, different rotor geometries and different auxiliary bearings sizes and locations can be easily taken into account.

Concerning the future developments of the work, the authors will improve the description of the coupling between the axial and the lateral dynamics of the system. Up to now, the authors considered the coupling between axial and lateral dynamics by studying the effect of axial dynamics on the lateral one. In the future, also the effect of lateral dynamics on the axial one will be investigated, especially in terms of axial forces and related vibrations. This way, a complete understanding of the phenomenon will be obtained.

Moreover, it could be interesting to develop a thermal and a wear model of the system. The thermal model could allow the monitoring of the temperature trend of the elements of the system, while the wear model could lead to an estimation of the wear conditions of the auxiliary bearing system after the emergency landings.

Finally, detailed three-dimensional (3D) multibody and flexible multibody models of the system will be developed to reach a higher level of accuracy, especially concerning the contacts description.

Data Availability

The data used to support the findings of this study are included within the article.

Conflicts of Interest

The authors declare that they have no conflicts of interest.

Acknowledgments

A special thank goes to the colleagues of "Baker Hughes, a GE company", for their support and assistance and for providing the test rig for the experimental tests.

References

[1] W. M. Szcygielski, *Dynamisches Verhalten Eines Schnell Drehenden Rotors Bei Anstreifvorgangen [Ph.D. thesis]*, Diss. ETH Nr 8094, ADAG Administration und Druck AG, Zurich, Switzerland, 1986.

[2] A. Muszynska, "Rotor-to-stationary element rub-related vibration phenomena in rotating machinery—literature survey," *The Shock and Vibration Digest*, vol. 21, no. 3, pp. 3–11, 1989.

[3] R. F. Beatty, "Differentiating rotor response due to radial rubbing," *Journal of Vibration, Acoustics, Stress, and Reliability in Design*, vol. 107, no. 2, p. 151, 1985.

[4] F. Ehrich, "Observations of subcritical superharmonic and chaotic response in rotordynamios," *Journal of Vibration and Acoustics*, vol. 114, no. 1, pp. 93–100, 1992.

[5] A. R. Bartha, *Dry Friction Induced Backward Whirl of Rotors [Dissertation thesis]*, Dissertation ETH No. 13817, ETH, Zurich, Switzerland, 2000.

[6] A. R. Bartha, "Dry friction induced backward whirl: theory and experiment," in *Proceedings of the 5th IFToMM Conference on Rotordynamics*, pp. 756–767, Darmstadt, Germany, 1998.

[7] J. C. Wilkes, D. W. Childs, B. J. Dyck, and S. G. Phillips, "The numerical and experimental characteristics of multimode dry-friction whip and whirl," *Journal of Engineering for Gas Turbines and Power*, vol. 132, no. 5, p. 052503, 2010.

[8] S. Lahriri, I. F. Santos, H. I. Weber, and H. Hartmann, "On the nonlinear dynamics of two types of backup bearings - Theoretical and experimental aspects," *Journal of Engineering for Gas Turbines and Power*, vol. 134, no. 11, 2012.

[9] J. Schmied and J. C. Pradetto, "Behaviour of a one ton rotor being dropped into auxiliary bearings," in *Proceedings of the Third International Symposium on Magnetic Bearings*, 1992.

[10] H. Xie, G. T. Flowers, L. Feng, and C. Lawrence, "Steady-state dynamic behavior of a flexible rotor with auxiliary support from a clearance bearing," *Journal of Vibration and Acoustics*, vol. 121, no. 1, pp. 78–83, 1999.

[11] L. D. Pietra, E. de Rosa, and C. Rossi, "Static and dynamic behaviour of a rigid rotor on journal bearings," *Meccanica*, vol. 26, no. 4, pp. 229–245, 1992.

[12] L. Hawkins, P. McMullen, and R. Larsonneur, "Development of an AMB energy storage flywheel for commercial applications," in *Proceedings of the 8th International Symposium on Magnetic Suspension Technology*, Dresden, Germany, 2005.

[13] P. McMullen, V. Vuong, and L. Hawkins, "Flywheel energy storage system with ambs and hybrid backup bearings," in *Proceedings of the 10th International Symposium on Magnetic Bearings (ISMB)*, Martigny, Switzerland, 2007.

[14] M. Dougdag, M. Ouali, H. Boucherit, N. E. Titouche, and M. Djaoui, "An experimental testing of a simplified model of a ball bearing: Stiffness calculation and defect simulation," *Meccanica*, vol. 47, no. 2, pp. 335–354, 2012.

[15] D. Ransom, A. Masala, J. Moore, G. Vannini, and M. Camatti, "Numerical and experimental simulation of a vertical high speed motorcompressor rotor drop onto ctcher bearings," in *Proceedings of the Eleventh International Symposium on Magnetic Bearings*, Nara, Japan, 2008.

[16] A. Masala, G. Vannini, D. Ransom, and J. Moore, "Numerical simulation and full scale landing test of a 12.5 MW vertical motorcompressor levitated by active magnetic bearings," in *Proceedings of the ASME TurboExpo*, Vancouver, Canada, 2011.

[17] R. G. Kirk, "Evaluation of AMB turbomachinery auxiliary bearings," *Journal of Vibration and Acoustics*, vol. 121, no. 2, p. 156, 1999.

[18] E. E. Swanson, R. G. Kirk, and J. Wang, "AMB rotor drop initial transient on ball and solid bearings," in *Proceedings of the Industrial Conference and Exhibition on Applications of Magnetic Bearings, Magnetic Drives, and Dry Gas Seals*, pp. 10-11, Alexandria, VA, USA, 1995.

[19] J. Wilkes, J. Moore, D. Ransom, and G. E. Vannini, "An improved catcher bearing model and an explanation of the forward whirl/whip phenomenon observed in active magnetic bearing transient drop experiments," in *Proceedings of the ASME Turbo Expo 2013: Turbine Technical Conference and Exposition, GT2013*, San Antonio, Tx, USA, 2013.

[20] G. Genta, *Dynamics of Rotating Systems*, Springer, 2005.

[21] M. I. Friswell, J. E. Penny, S. D. Garvey, and A. W. Lees, *Dynamics of Rotating Machines*, Cambridge University Press, Cambridge, UK, 2010.

[22] G. Genta, *Vibration of Structures and Machines*, Springer, New York, NY, USA, 2nd edition, 1993.

[23] T. Harris, *Rolling Bearing Analysis*, John Wiley & Sons, New York, NY, USA, 2nd edition, 1984.

[24] L. F. Shampine and M. W. Reichelt, "The MATLAB ODE suite," *SIAM Journal on Scientific Computing*, vol. 18, no. 1, pp. 1–22, 1997.